



**AIAA 98-3462**

**Modeling of Multiphase Alumina-Loaded Jet  
Flow Fields**

A. V. Rodionov and Yu. A. Plastinin

Central Research Institute for Machine Building  
(TSNIIMASH)

Korolev, Moscow Region, Russia 141070  
and

J. A. Drakes, M. A. Simmons, and R. S. Hiers, III  
Sverdrup Technology, Inc., AEDC Group  
Arnold Engineering Development Center  
Arnold Air Force Base, Tennessee 37389-6001

19991130 091

**34th AIAA/ASME/SAE/ASEE  
Joint Propulsion Conference & Exhibit  
July 13-15, 1998 / Cleveland, OH**

# Modeling of Multiphase Alumina-Loaded Jet Flow Fields\*

A. V. Rodionov, \*\*Yu. A. Plastinin, \*\*  
Central Research Institute for Machine Building  
(TSNIIIMASH)  
Korolev, Moscow Region, Russia 141070

and J. A. Drakes, † M. A. Simmons, †† and R. S. Hiers, II‡  
Sverdrup Technology, Inc., AEDC Group  
Arnold Engineering Development Center  
Arnold Air Force Base, TN 37389-6001

## Abstract

A computer program for simulating coupled phenomena of propulsion-generated, chemically reacting, two-phase jet flow fields is described in detail. A sample calculation is performed using typical solid-propellant rocket motor operating conditions as input. The model contains approximations for turbulence, particle drag, chemistry, and particle supercooling. The particle phase change is simulated kinetically and includes two solid  $\text{Al}_2\text{O}_3$  crystalline structures: meta stable gamma and stable alpha forms.

## Introduction

Accurate modeling of multiphase alumina-loaded rocket exhaust flow fields is essential for assessments of the missile base heat transfer to ensure the motor's health and survival. Two-phase gas/particle flow-field simulation is also an important element of efforts to predict solid-propellant rocket motor effluents for environmental studies including space debris. In order to assess the nominal performance of solid-propellant propulsion systems, two-phase simulations are essential. The condensed particulates stabilize the combustion chamber process and increase the combustion chamber temperatures; however, the drag introduced by the particulates in the expanding nozzle

represents a two-phase flow performance loss and a decrement to the thrust chamber performance. Thus, the presence of particulates in thrust chambers must be carefully evaluated in performance assessment methodologies. In reality, this problem presents a scenario in which a continuous range of solid, liquid, and multiple phase, i.e. liquid, as well as multiple-phase solid crystalline particulates, are spewed out within a hot bath gaseous mixture from the combustion chamber. Expansion of the exhaust gas acts as a spectator, tending the small particles to a higher velocity, and the larger particles to a higher internal energy (temperature). It is not surprising, then, that the implementation of known particle phase change kinetics presupposes an intrinsic coupling with the most up-to-date multiphase flow models.

Many standard models approach the problem using an equilibrium process to describe the phase change of thrust chamber-generated aluminum oxide ( $\text{Al}_2\text{O}_3$ ) particulates from liquid to solid as the flow expands and cools. In this approach, the liquid particle temperature is tracked until the melting temperature is reached. At this point, an equilibrium phase change process is initiated where the heat of fusion is released from the particulate to the lower temperature gas stream. The particulate temperature is maintained at the melting temperature until

\* The research reported herein was performed by the Arnold Engineering Development Center (AEDC), Air Force Materiel Command. Work and analysis for this research were performed by personnel of the Central Research Institute for Machine-Building (TSNIIIMASH) and by personnel of Sverdrup Technology, Inc., AEDC Group, technical services contractor for AEDC. Further reproduction is authorized to satisfy needs of the U. S. Government.

\*\* aaegk@glasnet.ru; (095) 513-4468.

† drakes@hap.arnold.af.mil; (931) 454-7694; Senior Member, AIAA.

†† simmons.martha@hap.arnold.af.mil; (931) 454-4658; Senior Member, AIAA.

‡ hiers@hap.arnold.af.mil; (931) 454-5820; Senior Member, AIAA.

Approved for public release; distribution unlimited.

the heat of melting is completely absorbed by the gas stream. At this point the particulates are in the stable solid alpha phase. In an expanding flow environment, the temperature of the solid particle will continue to decrease as the gas flow continues to expand and cool. This phase change model is an oversimplification because it does not account for the crystallization kinetics and the metastable gamma crystallization phase which have been experimentally observed in the laboratory during analyses of the phase change process. We have taken an alternate approach and have solved the equations of motion for all phases of the exhaust flow, including gas, liquid particles, particles of both liquid and solid phases, i.e., slush balls, and particles of multiple solid crystalline structures. The most significant advancement of this work relative to the industry standard is that the particle phase change process is kinetically controlled and includes the transition from metastable gamma crystalline structure to the stable alpha phase. This model also retains the essential physical character of particulate undercooling also observed in the laboratory.

### Mathematical Models

#### Gasdynamics

The system of gasdynamic equations for planar ( $v = 0$ ) or axisymmetric ( $v = 1$ ) flows can be written in the following form:

$$\frac{\partial \rho u}{\partial x} + \frac{\partial \rho v}{\partial y} + v \frac{\partial \rho}{\partial y} = 0 \quad (1)$$

$$\frac{\partial(\rho u^2 + P)}{\partial x} + \frac{\partial \rho u v}{\partial y} + v \frac{\partial \rho u}{\partial y} = F_u \quad (2)$$

$$\frac{\partial \rho u v}{\partial x} + \frac{\partial(\rho v^2 + P)}{\partial y} + v \frac{\partial \rho v}{\partial y} = F_v \quad (3)$$

$$\frac{\partial \rho u h_0}{\partial x} + \frac{\partial \rho v h_0}{\partial y} + v \frac{\partial \rho v h_0}{\partial y} = F_h \quad (4)$$

$$\frac{\partial \rho u q_n}{\partial x} + \frac{\partial \rho v q_n}{\partial y} + v \frac{\rho v q_n}{y} = \rho \Phi_n + F_n \quad (5)$$

Here  $x$  and  $y$  are the axes of a Cartesian system of coordinates,  $u$  and  $v$  are the velocity components in these coordinates,  $\rho$  and  $P$  are the density and the static pressure,  $h_0$  is the specific total enthalpy,  $q_n$  is an additional parameter which describes the nonequilibrium processes occurring in the gas mixture,  $\Phi$  is a term defined by the kinetic theory of nonequilibrium processes, and  $F$  is the term responsible for viscosity, heat conductivity, diffusion, and interaction with the particles.

#### Chemical Reactions

One assumes that there are several independent chemical reactions in a gas mixture. The form of the gas phase chemical reactions is as follows:

$$\sum_n C_{mn}^+ A_n = \sum_n C_{mn}^- A_n$$

where  $C_{mn}^+$  and  $C_{mn}^-$  are stoichiometric coefficients specifying the quantity of  $A_n$ , the chemical component taking part in the forward and reverse directions of the  $m^{\text{th}}$  reaction, respectively. Thus, as the result of  $m^{\text{th}}$  forward or reverse reaction,  $\Delta C_{mn} = C_{mn}^- - C_{mn}^+$ , molecules of  $A_n$  type are formed or destroyed.

For chemical kinetic equations, the mole-mass concentrations,  $\alpha_n$ , are chosen as  $q_n$ . The terms  $\Phi_n$  in the right-hand side of Eq. (5) have the form

$$\Phi_n = \frac{RT}{PM_{\Sigma}} \sum_m \Delta C_{mn} \left[ K_m^+ \prod_{n'} (P_{n'}/RT)^{C_{mn}^+} - K_m^- \prod_{n'} (P_{n'}/RT)^{C_{mn}^-} \right]$$

where  $T$  is the static temperature,  $M_{\Sigma} = 1/\sum \alpha_n$  is the molecular weight,  $R$  is the universal gas constant,  $P_n = r_n P$  is the partial pressure,  $r_n = M_{\Sigma} \alpha_n$  is the mole fraction, and  $K_m^+(T)$  and  $K_m^-(T)$  are the rate constants for the forward and reverse directions of the  $m^{\text{th}}$  reaction, respectively.

Table 1 includes the chemical rate equation and a set of chemical reactions and coefficients used to determine the rate constants for combustion products of the C-H-O-N-Cl type. They are chosen in accordance with Ref. 1, Vol. 1 and Ref. 2, Chapter 17. The reverse direction rate constants,  $K_m^-(T)$ , are defined using the equilibrium constants  $K_m(T) = K_m^+(T)/K_m^-(T)$  which are taken from Ref. 3.

### Laminar and Turbulent Mixing

For predictions of the viscous flow, the terms  $F_u^{\text{vis}}$  must be added to the right-hand side of Eqs. (2)-(5). In the parabolized Navier-Stokes equations<sup>4</sup> (where streamwise diffusive terms are eliminated), these terms can be written as

$$\begin{aligned} F_u^{\text{vis}} &= \frac{\partial U}{\partial y} + v \frac{U}{y}, \quad F_v^{\text{vis}} = \frac{\partial V}{\partial y} \\ F_h^{\text{vis}} &= \frac{\partial H}{\partial y} + v \frac{H}{y}, \quad F_n^{\text{vis}} = \frac{\partial Q_n}{\partial y} + v \frac{Q_n}{y} \\ U &= \left(1 + \frac{v^2}{u^2}\right) \left(\mu + \mu_t\right) \frac{\partial u}{\partial y} \\ V &= \left(1 + \frac{v^2}{u^2}\right) \left(\mu + \mu_t\right) \frac{\partial v}{\partial y} \\ Q_n &= \left(1 + \frac{v^2}{u^2}\right) \left(\frac{\mu}{Pr} + \frac{\mu_t}{Pr_t}\right) \frac{\partial q_n}{\partial y} \\ H &= \left(1 + \frac{v^2}{u^2}\right) \left[ \left(\mu + \mu_t\right) \frac{\partial h_0}{\partial y} + \left(\frac{\mu}{Pr} + \frac{\mu_t}{Pr_t} - \mu - \mu_t\right) \frac{\partial h}{\partial y} \right] \end{aligned} \quad (6)$$

Here,  $\mu = \mu(T, q)$  and  $\mu_t$  are the laminar and turbulent viscosity coefficients,  $h = h(T, q)$  is the specific static enthalpy, and  $Pr$  and  $Pr_t$  are the laminar and turbulent Prandtl numbers. In Eq. (6) one assumes that the laminar and turbulent Schmidt numbers are equal,  $Sc = Pr$  and  $Sc_t = Pr_t = 0.7$ . The term  $(1 + v^2/u^2)$  is inserted into the equations to take account of the shear layer inclination with respect to the  $x$  axis.

In turbulent flow analysis,  $u$ ,  $v$ ,  $\rho$ , and  $P$  are treated as the Favre-averaged values. A variant of the  $\kappa-\epsilon$  turbulence model suggested in Ref. 4 is

Table 1. Chemical Reactions and Rate Constants  
 $K^+ = AT^{-n} \exp(-E/RT)$

Reaction	$A, m^6/(kmol \cdot sec)^2$	$n$	$E, cal$
$CO + O + M = CO_2 + M$	$3.5 \cdot 10^8$	0	2100
$OH + H + M = H_2O + M$	$1.2 \cdot 10^{14}$	1	0
$O + N + M = NO + M$	$3.3 \cdot 10^9$	0	0
$H + H + M = H_2 + M$	$1.4 \cdot 10^{14}$	1.5	0
$O + O + M = O_2 + M$	$5.5 \cdot 10^{11}$	0.87	0
$N + N + M = N_2 + M$	$2.7 \cdot 10^{10}$	0.5	0
$H + O + M = OH + M$	$3.3 \cdot 10^{12}$	0.5	0
$Cl + Cl + M = Cl_2 + M$	$3.6 \cdot 10^8$	0	-1800
$H + Cl + M = HCl + M$	$1.4 \cdot 10^{16}$	2	0
Reaction	$A, m^3/kmol \cdot sec$	$n$	$E, cal$
$OH + CO = CO_2 + H$	$2.5 \cdot 10^9$	0	5100
$H_2 + OH = H_2O + H$	$1.1 \cdot 10^{11}$	0	8600
$OH + OH = H_2O + O$	$1.0 \cdot 10^{10}$	0	1200
$H_2 + O = OH + H$	$1.3 \cdot 10^{10}$	0	9860
$O_2 + H = OH + O$	$2.2 \cdot 10^{11}$	0	16,500
$O_2 + N_2 = NO + NO$	$5.2 \cdot 10^{10}$	0	107,000
$NO + N = N_2 + O$	$3.0 \cdot 10^{10}$	0	200
$NO + O = O_2 + N$	$1.1 \cdot 10^{10}$	0	41,700
$Cl + H_2 = HCl + H$	$8.4 \cdot 10^9$	0	4260
$Cl + H_2O = HCl + OH$	$3.0 \cdot 10^{10}$	0	17,600
$HCl + O = OH + Cl$	$3.6 \cdot 10^{10}$	0	6000
$H + Cl_2 = HCl + Cl$	$9.0 \cdot 10^{10}$	0	1200

used for  $\mu_t$  determination. Equations for the kinetic energy of turbulence ( $\kappa$ ) and its dissipation ( $\epsilon$ ) coincide with Eq. (5) if  $F$  and  $\Phi$  are defined by

$$\begin{aligned} F_{\kappa}^{\text{vis}} &= \frac{\partial K}{\partial y} + v \frac{K}{y}, \quad F_{\epsilon}^{\text{vis}} = \frac{\partial E}{\partial y} + v \frac{E}{y} \\ K &= \left(1 + \frac{v^2}{u^2}\right) \left(\mu + \mu_t\right) \frac{\partial \kappa}{\partial y} \\ E &= \left(1 + \frac{v^2}{u^2}\right) \left(\mu + \frac{\mu_t}{1.3}\right) \frac{\partial \epsilon}{\partial y} \\ \Phi_{\kappa} &= \frac{\mu_t}{\rho} \left[ \left(1 + \frac{v^2}{u^2}\right) \frac{\partial u}{\partial y} \right]^2 - \epsilon (1 + C_1) \\ \Phi_{\epsilon} &= \frac{\epsilon}{\kappa} \left\{ 1.43 \frac{\mu_t}{\rho} \left[ \left(1 + \frac{v^2}{u^2}\right) \frac{\partial u}{\partial y} \right]^2 - \epsilon (C_2 + C_1) \right\} \end{aligned} \quad (7)$$

where

$$C_1 = \min(1.32, 0.3M_t + 7.5M_t^2), \quad M_t = \sqrt{\kappa\rho/\gamma P}$$

$$C_2 = 1.92 - 0.0667f$$

Here,  $\gamma$  is the specific heat ratio and  $f$  is set to zero in the region extended axially from the nozzle

exit to the cross section where the shear (mixing) layer reaches the x axis. Downstream of that cross section location,  $f$  is defined by

$$f = \left| \frac{y_1}{(u_e - u_0)} \frac{du_0}{dx} \right|^{0.2}$$

where  $u_0$  and  $u_e$  are the gas velocities at the x axis and the external flow velocity, respectively. Turbulent viscosity coefficient is defined by

$$\mu_t = C_\mu \frac{\kappa^2 [1 - 0.222(1 + C_1)]}{\epsilon} \frac{0.78}{0.78}$$

where  $C_\mu = 0.09 - 0.04f$

### Thermodynamics

The specific total enthalpy is defined by

$$h_0 = (u^2 + v^2)/2 + \kappa + h, h = \sum_n \alpha_n h_n$$

where  $h_n = h_n(T)$  is the mole enthalpy of the  $n^{\text{th}}$  chemical component, including its formation heat. These enthalpies are taken from the reference handbook.<sup>3</sup>

The specific heat ratio,  $\gamma$ , for gaseous mixtures is understood to be "frozen" and defined by

$$\gamma = \frac{C_p}{C_v}, C_p = \frac{\partial h}{\partial T} \Big|_{q=\text{const}}, C_v = C_p - \frac{R}{M_\Sigma}$$

The equation of state has the form

$$P = \frac{\rho RT}{M_\Sigma}$$

However, the  $\kappa-\epsilon$  turbulence model<sup>4</sup> requires that the additional pressure of turbulent pulsation be included in the momentum Eqs. (2) and (3). Because of this, the value  $P$  will be understood as the sum of both the static and additional pressures created by turbulent pulsations. Therefore, the equation of state should be rewritten in the form:

$$P = \frac{\rho RT}{M_\Sigma} + \hat{P}, \hat{P} = \frac{2}{3} \rho \kappa [1 - 0.222(1 + C_1)]$$

### Liquid/Solid Phase (Particles)

The mathematical modeling of multiphase flows in the context of multitemperature and multivelocitity simulations must invoke additional equations describing the motion of  $\text{Al}_2\text{O}_3$  particles, including the particle phase thermodynamics and kinetics. Under the assumptions that the particles are spherical, chemically inert to the gaseous phase, and do not interact with each other, these equations can be written as:

$$\frac{du_s}{dt} = C_f(u - u_s), \frac{dv_s}{dt} = C_f(v - v_s) \quad (8)$$

$$\frac{de_s}{dt} = C_q(T - T_s) \quad (9)$$

where

$$C_f = \frac{3C_d \rho W_s}{8r_s \rho_s^0}, C_d = C_d(Re_s, M_s, \gamma, T_s/T)$$

$$C_q = \frac{3Nu\lambda}{2\rho_s^0 r_s^2}, Nu = \frac{Nu^0}{1 + 3.42Nu^0 M_s/Re_s Pr}$$

$$Nu^0 = 2 + 0.459Re_s^{0.55} Pr^{0.33}, M_s = \frac{W_s}{a}$$

$$Re_s = \frac{2W_s \rho r_s}{\mu}, W_s = \sqrt{(u - u_s)^2 + (v - v_s)^2}$$

Here index 's' denotes the number of particle fractions (all particles from each fraction are of the same size),  $u_s$  and  $v_s$  are the particle velocity components,  $d/dt \equiv u_s \partial/\partial x + v_s \partial/\partial y$  is the total derivative with respect to the time (along the particle trajectory),  $e_s$  and  $T_s$  are the specific internal energy and the temperature of particles, respectively,  $r_s$  is the particle radius,  $\rho_s^0 = 3329 \text{ kg/m}^3$  is the intrinsic density of alumina material,  $\lambda$  and  $\mu$  are the heat conductivity and the viscosity of the surrounding gas, and  $a = \sqrt{\gamma(P/\rho)}$  is the gas sound velocity. Unitless drag coefficient of particles,  $C_d$ , is defined by relationships given in Ref. 5.

**Nonequilibrium crystallization.**\* As  $\text{Al}_2\text{O}_3$  particle temperatures in the nozzle and exhaust jet decrease, they experience the liquid-to-solid phase transition process releasing the crystallization energy. This is a nonequilibrium process which is described using the relative crystallization front radius,  $r_s^*$ . A particle entirely in the liquid state is denoted by  $r_s^* = 1$ , whereas  $r_s^* = 0$  corresponds to the complete solid state. If the particle is in the transitional state, then  $0 < r_s^* < 1$ , and the kinetic recession of the crystallization front is described by the equation

$$r_s \frac{dr_s^*}{dt} = -a^* (T_m - T_s)^{1.8} \quad (10)$$

where  $a^* = 0.64 \cdot 10^{-6} \text{ m/sec} \cdot \text{K}^{1.8}$  and  $T_m = 2289 \text{ K}$ , the equilibrium melting temperature. According to the adopted model, particle crystallization begins just below the critical temperature,  $T_c = 0.83T_m$  (1900 K).<sup>6,7</sup> The liquid phase is assumed to transfer initially to the metastable solid  $\gamma$  phase for all conditions. The transition process from the  $\gamma$  phase to the stable  $\alpha$  phase begins as soon as any portion of the  $\gamma$  phase has appeared. To determine the portion of solid substance in the  $\alpha$  phase ( $f_\alpha$ ), the following equation is applied<sup>8</sup>:

$$\frac{df_\alpha}{dt} = a_\alpha \exp(-b_\alpha/T_s) \quad (11)$$

where  $a_\alpha$ ,  $b_\alpha$  are empirical coefficients. According to measurements<sup>9</sup> and recommendations,<sup>8</sup>  $b_\alpha = 58,368 \text{ K}$ . The value of  $a_\alpha$  is chosen to be equal to  $1.5 \cdot 10^{12} \text{ 1/sec}^{10}$ .

While the solid phase portion of the particle is known, the total portions of the  $\gamma$  phase ( $M_\gamma$ ) and the  $\alpha$ -phase ( $M_\alpha$ ) are defined by formulae

$$M_\gamma = \left(1 - (r_s^*)^3\right)(1 - f_\alpha), \quad M_\alpha = \left(1 - (r_s^*)^3\right)f_\alpha$$

The specific internal energy,  $e_s$ , is connected with the particle temperature,  $T_s$ , by the equation

$$e_s = C_s T_s + h_s (r_s^*)^3$$

where  $h_s = 0.915 \cdot 10^6 \text{ J/kg}$  is the latent heat of the  $\text{Al}_2\text{O}_3$  fusion and  $C_s = 1600 \text{ J/kg} \cdot \text{K}$  is the specific heat capacity of particles. Here, the coefficient  $C_s$  is assumed to be equal for both the liquid and solid states. Furthermore, one assumes an equal value of  $\rho_s^0$  for both states. This implies that the radius of each particle remains unchanged along the trajectory.

**Equilibrium crystallization.** Assuming an equilibrium liquid-to-solid transition process readily connects the specific internal energy,  $e_s$ , to the temperature of particles,  $T_s$ , by the following relation:

$$T_s = \begin{cases} e_s/C_s, & \text{if } e_s < C_s T_m \\ T_m, & \text{if } C_s T_m < e_s < C_s T_m + h_s \\ (e_s - h_s)/C_s, & \text{if } C_s T_m + h_s < e_s \end{cases}$$

**Influence on gas.** Eqs. (8) and (9) describe the changes in momentum and internal energy of particles immersed in gaseous flow. The particles' effect on the gas is taken into account by terms  $F^{\text{part}}$ , which have the following form:

$$\begin{aligned} F_u^{\text{part}} &= \sum_s \rho_s C_f (u_s - u) \\ F_v^{\text{part}} &= \sum_s \rho_s C_f (v_s - v) \\ F_h^{\text{part}} &= \sum_s \rho_s \{ C_f [u_s(u_s - u) + v_s(v_s - v)] \\ &\quad + C_q (T_s - T) \} \end{aligned} \quad (12)$$

where  $\rho_s$  is the mass density of the particle cloud. To define  $\rho_s$ , one invokes the continuity equation of a particle cloud

$$\frac{d\rho_s u_s S_s}{dt} = 0$$

where  $S_s$  is the area of the particle flow-tube.

\*The mathematical description of  $\text{Al}_2\text{O}_3$  particle kinetics has been given previously in Ref. 10.

## Numerical Techniques

The system of equations describing the gas and particle flow properties is solved by using axial marching numerical methods; that is, passing from one cross section  $x = x^k \equiv \text{const}$  to another, step by step as  $K$  is monotonically increased ( $k = 0, 1, 2, \dots$ ).

Passing from cross section  $x = x^k$  to  $x = x^{k+1}$  (one step) involves several iterations which included split computations of gas and particle parameters. Within one iteration the gas parameters are computed with the particle interaction terms,  $F^{\text{part}}$ , taken from the previous iteration. Then particle parameters are calculated using the previously obtained gas parameters. After that, particle interaction terms are recomputed to be used in the next iteration. In practice, only two iterations of this type are needed to define all gas and particle properties.

## Calculation of Gas Parameters

To compute the gas parameters within one iteration, the numerical technique described in detail in Ref. 11 is applied. This technique invokes the same assumptions as the SCIPVIS technique<sup>12</sup> and allows space-marching calculation of the subsonic regions (e.g., subsonic external flow and flow regions behind the Mach disc). An original second-order Godunov method fitted to the coupled calculation of sub- and supersonic regions is used to integrate gasdynamic and kinetic equations without using a splitting technique. An explicit-implicit approximation of source terms ( $\Phi_n$ ) on the right-hand side of kinetic Eqs. (5) provides a stable computation of fast-relaxing flows.

According to the adopted method, the distributions of gas parameters ( $u, v, p, P, h_0, q_n$ ) at any cross section  $x = x^k$  are described by piecewise-linear functions with discontinuities at the grid points  $y_j^k$  ( $j = 0, 1, \dots, J$ ;  $y_0^k < y_1^k < \dots < y_J^k$ ). These grid points are used for the gas parameter computations only.

## Calculation of Particle Parameters

This section describes a numerical technique for computation of Eqs. (8)-(11) within one iteration between the first ( $x = x^k$ ) and the second ( $x = x^{k+1}$ ) cross sections.

Let us consider several trajectories of the  $s^{\text{th}}$  particle fraction. These trajectories have numbers  $js = 1, 2, \dots, Js$ . At the first section, the trajectory coordinates,  $y_{js}^k$ , and the particle parameters  $(u_s, v_s, e_s, r_s^*, f_\alpha)_{js}^k$  at these points are considered to be known. The gas parameter distributions are known at both  $x = x^k$  and  $x = x^{k+1}$  sections.

At the second section the trajectory coordinates,  $y_{js}^{k+1}$ , and the particle velocity components,  $(u_s, v_s)_{js}^{k+1}$ , are calculated by the following formulae:

$$y_{js}^{k+1} = y_{js}^k + \frac{(v_s)_{js}^k + (v_s)_{js}^{k+1}}{(u_s)_{js}^k + (u_s)_{js}^{k+1}} \Delta x$$

$$(u_s)_{js}^{k+1} = \frac{(u_s)_{js}^k + 0.5 \Delta t \hat{C}_f [u_{js}^k + u_{js}^{k+1} (1 + \Delta t \hat{C}_f)]}{1 + \Delta t \hat{C}_f (1 + 0.5 \Delta t \hat{C}_f)}$$

$$(v_s)_{js}^{k+1} = \frac{(v_s)_{js}^k + 0.5 \Delta t \hat{C}_f [v_{js}^k + v_{js}^{k+1} (1 + \Delta t \hat{C}_f)]}{1 + \Delta t \hat{C}_f (1 + 0.5 \Delta t \hat{C}_f)}$$

where  $\hat{C}_f = 0.5 [(C_f)_{js}^k + (C_f)_{js}^{k+1}]$ ,  $\Delta x = x^{k+1} - x^k$ ,  $\Delta t = (2 \Delta x) / [(u_s)_{js}^k + (u_s)_{js}^{k+1}]$ . The particle parameters at the second section,  $x = x^{k+1}$ , appearing in the right-hand side of these equations are taken from the previous iteration. The gas parameters  $(u_{js}^k, u_{js}^{k+1}, \dots)$  at both sections are defined at the particle trajectory points.

In the part of the trajectory where crystallization does not hold (either  $r_s^* = 1$  and  $T_s > T_c$  or  $r_s^* = 0$ ) the particle temperature is calculated by

$$(T_s)_{js}^{k+1} = \frac{(T_s)_{js}^k + 0.5 \Delta t \frac{\hat{C}_q}{C_s} \left[ T_{js}^k + T_{js}^{k+1} \left( 1 + \Delta t \frac{\hat{C}_q}{C_s} \right) \right]}{1 + \Delta t \frac{\hat{C}_q}{C_s} \left( 1 + 0.5 \Delta t \frac{\hat{C}_q}{C_s} \right)}$$

where  $\hat{C}_q = 0.5 \left[ (C_q)_{js}^k + (C_q)_{js}^{k+1} \right]$ .

In the part of the trajectory where crystallization occurs, Eqs. (9) and (10) are integrated using small step size,  $\Delta t' \equiv \Delta k \Delta t$  ( $0 < \Delta k < 1$ ), successively passing from the point  $k' = k$  to the point  $k' = k + 1$ , using an explicit approach:

$$(e_s)_{js}^{k'+\Delta k} = (e_s)_{js}^{k'} + \hat{C}_q \left[ T_{js}^{k'} - (T_s)_{js}^{k'} \right] \Delta t'$$

$$(r_s^*)_{js}^{k'+\Delta k} = (r_s^*)_{js}^{k'} - \frac{a^*}{r_s} \left[ T_m - (T_s)_{js}^{k'} \right]^{1.8} \Delta t'$$

where the integration step,  $\Delta t'$ , satisfies the condition

$$\left| (T_s)_{js}^{k'+\Delta k} - (T_s)_{js}^{k'} \right| \leq 0.25 \left| T_m - (T_s)_{js}^{k'} \right|$$

$$0 \leq (r_s^*)_{js}^{k'+\Delta k} \leq 1$$

In the presence of  $\gamma$  phase ( $r_s^* < 1$  and  $f_\alpha < 1$ ), Eq. (11) is integrated explicitly

$$(f_\alpha)_{js}^{k+1} = \min \left\{ 1, (f_\alpha)_{js}^k + \Delta t a_\alpha \exp \left[ -b_\alpha / (T_s)_{js}^k \right] \right\}$$

### Calculation of Gas-Particle Interaction Terms

The following describes an approximation of gas particle interaction terms,  $F^{\text{part}}$ .

Mass expansion of the  $s^{\text{th}}$  particle fraction between the neighboring trajectories is expressed by:

$$\Psi_{js+1/2} = \left| \int_{y_{js}^k}^{y_{js+1}^k} (2\pi y)^v \rho_s u_s dy \right|$$

The values of  $\Psi_{js+1/2}$  are specified at the initial section,  $x = x^0$ , in compliance with the problem conditions. By Eq. (2.13), these values are not changed in the marching computation progression; that is, they are the same for any section  $x = x^k$ .

After calculation of the particle parameters at the second section,  $x = x^{k+1}$ , the following parameters describing gas particle interaction are defined

$$(f_u)_{js}^{k+1/2} \equiv \left[ \frac{C_f (u_s - u)}{u_s} \right]_{js}^{k+1/2} = \frac{(u_s)_{js}^k - (u_s)_{js}^{k+1}}{\Delta x}$$

$$(f_v)_{js}^{k+1/2} \equiv \left[ \frac{C_f (v_s - v)}{u_s} \right]_{js}^{k+1/2} = \frac{(v_s)_{js}^k - (v_s)_{js}^{k+1}}{\Delta x}$$

$$(f_h)_{js}^{k+1/2} \equiv \left\{ \frac{C_f [u_s (u_s - u) + v_s (v_s - v)]}{u_s} \right.$$

$$\left. + \frac{C_q (T_s - T)}{u_s} \right\}_{js}^{k+1/2} = (u_s f_u + v_s f_v)_{js}^{k+1/2}$$

$$+ \frac{(e_s)_{js}^k - (e_s)_{js}^{k+1}}{\Delta x}$$

$$\text{where } (u_s)_{js}^{k+1/2} = 0.5 \left[ (u_s)_{js}^k + (u_s)_{js}^{k+1} \right], (v_s)_{js}^{k+1/2} = 0.5 \left[ (v_s)_{js}^k + (v_s)_{js}^{k+1} \right].$$

So, we need to compute the gas-particle interaction terms,  $(F^{\text{part}})_{j+1/2}^{k+1/2}$ , at the centers of the elementary cells used for the gas parameter computations. Thus, let us consider the intermediate section,  $x = x^{k+1/2} = 0.5(x^k + x^{k+1})$ . In this section there are grid points  $y_j^{k+1/2} = 0.5(y_j^k + y_j^{k+1})$  which define the intervals  $(y_j^{k+1/2}, y_{j+1}^{k+1/2})$ . We will treat  $(F^{\text{part}})_{j+1/2}^{k+1/2}$  as the interaction terms averaged over these intervals.

We know that the particle trajectories  $y_{js}^{k+1/2} = 0.5(y_{js}^k + y_{js+1}^{k+1/2})$  at the intermediate section do not coincide with  $y_j^{k+1/2}$ . Furthermore, the gas-particle interaction terms averaged over intervals  $(y_{js}^{k+1/2}, y_{js+1}^{k+1/2})$  can be approximated by (hereafter the upper index,  $k+1/2$ , is omitted)

$$(F_u^{\text{part}})_{js+1/2} = \frac{\Psi_{js+1/2} [(f_u)_{js} + (f_u)_{js+1}]}{2[\pi(y_{js} + y_{js+1})]^v |y_{js+1} - y_{js}|}$$

$$(F_v^{\text{part}})_{js+1/2} = \frac{\Psi_{js+1/2} [(f_v)_{js} + (f_v)_{js+1}]}{2[\pi(y_{js} + y_{js+1})]^v |y_{js+1} - y_{js}|}$$

$$\left( F_h^{\text{part}} \right)_{js+1/2} = \frac{\Psi_{js+1/2} [(f_h)_{js} + (f_h)_{js+1}]}{2[\pi(y_{js} + y_{js+1})]^v |y_{js+1} - y_{js}|}$$

By this means, the problem is how to compute  $(F^{\text{part}})_{j+1/2}$ , knowing  $(F^{\text{part}})_{js+1/2}$  for each particle fraction. The trajectories of two particles in the same size group may intersect, with the only change being the reversal of index of radial location for the two particle.

A convenient way to solve this problem is to compute the value of  $(F^{\text{part}})_{j+1/2}(y_{j+1} - y_j)$  as the sum of all values of  $(F^{\text{part}})_{js+1/2}|y_{js+1} - y_{js}|$ , in full or in part, for which the interval  $(y_{js+1}, y_{js})$  is totally incorporated into the interval  $(y_{j+1}, y_j)$ , (the value in full) or intersects with it (the value in part). If the latter is the case, part of this value is defined by the expression:

$$\frac{(y_{\max} - y_{\min})}{|y_{js+1} - y_{js}|} \times \frac{(f.)_{\max} + (f.)_{\min}}{(f.)_{js+1} + (f.)_{js}}$$

where  $f. = f_u, f_v$  or  $f_h$ ,

$$y_{\max} = \min[y_{j+1}, \max(y_{js}, y_{js+1})],$$

$$y_{\min} = \max[y_j, \min(y_{js}, y_{js+1})]$$

$(f.)_{\max}$  and  $(f.)_{\min}$  are calculated at the points  $y_{\max}$  and  $y_{\min}$  by linear interpolation between  $(f.)_{js}$  and  $(f.)_{js+1}$ .

This procedure gives a correct approximation of  $(F^{\text{part}})_{j+1/2}$  for all cases of particle trajectory behaviors.

### Program Implementation

The described mathematical models and numerical techniques have been embodied in the software package, hereafter referred to as Numerical Analysis of Real Jets (NARJ).

NARJ is designed for the numerical simulation of two-dimensional steady outflow of propellant combustion products from chemical propulsion

devices. NARJ embraces the computations of gas/particle two-phase flow in

- Sub-, trans-, and supersonic parts of the classical converging/diverging nozzles;
- Jets exhausted from the nozzle into subsonic or supersonic external gas flow or into vacuum free-stream conditions.

NARJ consists of a large number of partially interconnected programs (written in *Fortran*), each solving specific problems for specified combustion products. NARJ includes physical-chemical approximations for chemical reactions, vibrational relaxation, homogeneous condensation, and laminar and turbulent mixing, and liquid-solid particle phase change kinetics. Interfacing of the modules is required to:

- utilize output data from one program as an input data to the other program;
- partially utilize the same program modules when forming different programs.

### Comparative Analysis

A sample calculation was performed, applying the NARJ computer program. The calculation was initiated with one-dimensional startline conditions at the nozzle exit plane, as described in Tables 2 and 3. These conditions represent a generic, solid-propellant rocket motor (SRM) with aluminum loading of approximately 20 percent. The fuel-rich composition of the exhaust gas, provided in Table 3, is also typical for SRM operation. The nozzle exit radius, denoted as  $R_e$ , was specified to be 1 foot.

In order to isolate and compare the modeling methodologies for the particle crystallization and gas/particle coupling, the particles and gaseous mixture were assumed to be initially equilibrated, having equal temperature and velocity. The initial temperature was assumed to be 2,500 K, well

Table 2. One-Dimensional Nozzle Exit Startline Conditions for NARJ Plume Simulation

Static Pressure	0.4 atm (5.9 psia)
Static Temperature*	2,500 K (4500°R)
Axial Velocity*	2895 m/sec (9498 ft/sec)
Mach number	2.35
Radial Velocity*	0.0 m/sec
Al <sub>2</sub> O <sub>3</sub> Density of each Size Group	9.07 × 10 <sup>-6</sup> gm/cm <sup>3</sup>
Particle Radii**	
Group 1	1.5 μm
Group 2	3.0 μm
Group 3	6.0 μm

\* The gas and the particulates were initially assumed to be in thermodynamic equilibrium having equal temperature and velocity at the nozzle exit.

\*\* All particulates are assumed to be spherical.

Table 3. Startline Gaseous Species Mole Fractions for NARJ Plume Simulation

CO	0.2862
CO <sub>2</sub>	0.01073
Cl	1.237E-3
Cl <sub>2</sub>	0.000
H	5.109E-3
H <sub>2</sub>	0.4139
H <sub>2</sub> O	7.409E-2
HCl	0.1319
N <sub>2</sub>	7.670E-2
O	1.628E-7
OH	6.408E-5
O <sub>2</sub>	0.000

above the assumed NARJ Al<sub>2</sub>O<sub>3</sub> particle solidification temperature of 2,289 K. Therefore, all the particulates were initially in the liquid phase. The NARJ model includes particulate supercooling approximation. The supercooling temperature is specified as approximately 1,900 K. All particle groups are expected to experience the liquid-to-solid phase change process as the plume exhaust expands and cools. Three particle size groups were included in these computations. The radii of the particle size groups are typical for SRM flows and are given in Table 2. The mole fraction composition of the exhaust gas mixture is shown in Table 3. The mass percentage of Al<sub>2</sub>O<sub>3</sub> particulates was approxi-

mately 44 percent of the total mass, equally divided among the three particle size groups.

The free-stream ambient flow conditions were specified as 0.1 atm (1.46 psia), providing an underexpanded nozzle operating condition with  $P_{exit}/P_{\infty} = 4$ . The free-stream velocity was specified as 1,100 m/sec (3,609 ft/sec). The static temperature was 217 K (390.6°R), corresponding to a flight Mach number of 3.7. The composition of the ambient airstream was specified by mole fractions as [N<sub>2</sub>] = 0.7897, [O<sub>2</sub>] = 0.2100, and [CO<sub>2</sub>] = 3.0 × 10<sup>-4</sup>.

In this analysis, two NARJ solutions were computed. The first solution used the default NARJ chemical kinetic rate data, based largely on Russian literature results. For the second solution, results were obtained using a modified version of NARJ, which contained a set of chemical reactions and rates taken from Baulch.<sup>13</sup> The intent of the second solution was to examine the impact of the rates of the Russian literature as compared to those of the western literature.

The calculated gas static temperature contours obtained from the default NARJ model are shown in Fig. 1. The computational domain of Fig. 1 extends axially from the nozzle exit to 20 R<sub>e</sub> downstream. The atmospheric gas entrainment and mixing with the plume gases contributes to the shear layer development, which is evident near the outer periphery of the contour map. The shear layer is delineated from the inviscid core flow by the tem-

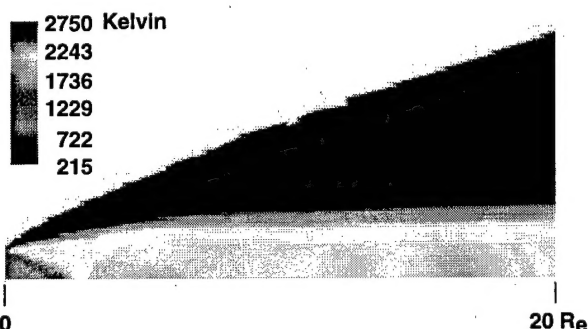


Fig. 1. Spatial map of default NARJ solution for the gas temperature.

perature gradient showing a region of elevated temperatures in the outer radial expansion region. Combustion and shear heating contribute to the temperature gradient in the shear layer. The one-dimensional, inviscid core flow is evident near the nozzle exit, and persists, undisturbed, along the centerline for approximately 1 nozzle radius.

Figure 2 is the static pressure contour map for the same nearfield segment of the NARJ computation. The rapid expansion of the underexpanded plume exhaust near the nozzle lip is evident. An inviscid wave structure emanating in the near-field region is evident and can be tracked as it propagates and reflects off the plume centerline and the plume outer boundary. This wave propagation is also observed in the gas temperature map of Fig. 1 as elevated temperatures along the centerline, 10  $R_e$  downstream.

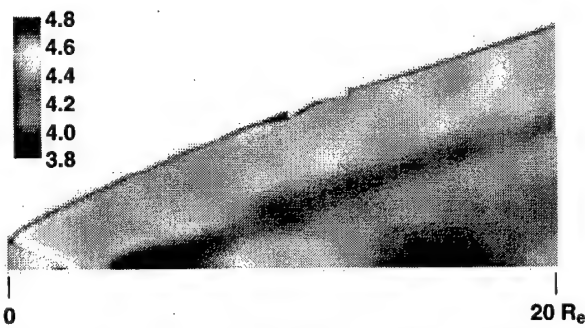


Fig. 2. Spatial map of default NARJ solution for the logarithm of the gas pressure in Pascals.

Fig. 3 is the calculated contour map of  $H_2O$  mole fraction showing the kinetic rate determination of  $H_2O$  concentration using the NARJ default chemistry. The factor of 2 increase in the  $H_2O$  mole fraction evident in comparing the initial  $H_2O$  mole fraction level to the shear layer  $H_2O$  mole fraction value indicates significant combustion resulting in formation of  $H_2O$  in the shear layer. The formation of  $H_2O$  in the shear layer results from ambient  $O_2$  entrainment, mixing, and combustion with the excess  $H_2$  in the plume exhaust gas mixture. It is interesting to note the very gradual initial development of the

shear layer and the accompanying combustion zone. Initially, there is very little production of  $H_2O$  near the nozzle lip, where the ambient air is not sufficiently entrained and the mixing is slight.



Fig. 3. Spatial map of default NARJ solution for the  $H_2O$  mole fraction.

Figure 4 is the centerline axial profile of  $H_2$ ,  $H_2O$ , and  $N_2$  mole fractions, showing the creation of  $H_2O$  and the corresponding  $H_2$  depletion and the mixing of the atmospheric  $N_2$  with the plume gases. The centerline static temperature of the gas is also included on Fig. 4. The afterburning shear layer appears to reach the plume centerline position at roughly  $50 R_e$ , as indicated by the presence of the  $N_2$  from the ambient air, and extends considerably into the far field, to roughly  $300 R_e$ . The increase in the temperature, followed by the gradual decrease in this region, is also indicative of shear layer combustion. Downstream of the location of air entrainment on the centerline, the core

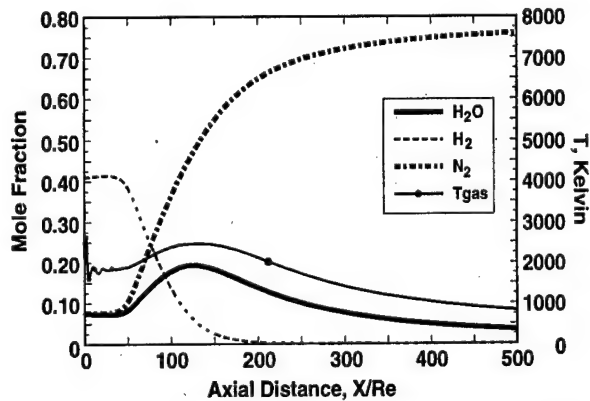


Fig. 4. Axial profiles of the default NARJ jet centerline properties.

flow field is dominated by mixing and combustion until the excess  $H_2$  is depleted near  $200 R_e$ .

As suggested in the previous description of the NARJ model, simulation of the coupled  $Al_2O_3$  particulate properties, including drag, trajectory, and phase change thermodynamics constitutes an essential portion of the computation methodology. Near-field particle temperature contours for the 1.5- $\mu m$  radius particle group is shown in Fig. 5. This contour map focuses on the near field region of the computational domain, extending axially to  $20 R_e$ . The small particulates experience the smallest drag force per particle and are nearly in equilibrium with the gas. As such, small particulates display a fairly rapid cooling trend similar to the gas phase temperature trend (shown previously in Fig. 1). The small particles track the gas flow in the shear layer and are heated by the combustion taking place in this region. The particle temperatures also increase in the downstream region near the centerline. This sudden temperature rise near the centerline is due to the phase change "blik" phenomenon that results when the supercooled liquid particulates rapidly transition to the metastable gamma solid phase, accompanied by a rapid rise in temperature. This phenomenon is also evident in Fig. 6, a contour map of the solid metastable gamma crystalline phase fraction for the 1.5- $\mu m$   $Al_2O_3$  particulates.

The liquid phase is prevalent in the near-field region of the jet, as expected since the particles were initiated in the liquid phase. The first occurrence of the metastable gamma solid phase is downstream near the centerline, where the super-

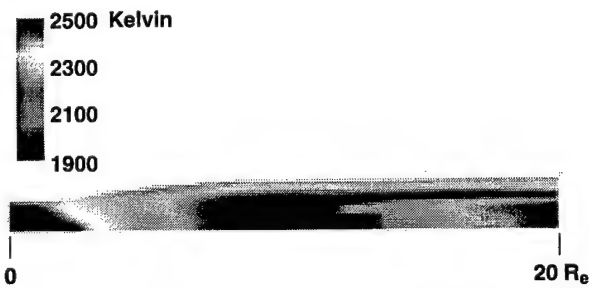


Fig. 5. Spatial map of default NARJ solution for the temperature of the 1.5- $\mu m$  particle group.



Fig. 6. Spatial map of default NARJ solution for the gamma phase fraction of the 1.5- $\mu m$  particle group.

cooling temperature "blik" phenomenon occurs. As soon as the particle supercooling temperature is realized, the transition process from liquid to metastable gamma crystalline structure begins, coincident with the kinetically controlled transition from the metastable gamma to the stable alpha crystalline structure. The spatial distribution of the alpha phase fraction for this particle group is shown in Fig. 7. As expected, the alpha phase formation occurs within the same spatial region as the gamma phase. The alpha phase production rate is extremely temperature sensitive, decreasing by nearly 6 orders of magnitude as the temperature declines from the solidification temperature of 2,289 K to 1,500 K. Therefore, the majority of the formation of alpha phase occurs in the spatial region immediately following the particle "blik," where the particles are initially solidified at relatively high temperatures. Overall, the crystalline phase transition process does not appear to influence the gas dynamic behavior of any portion of the flow. However, differences in the solid phase crystalline structure could influence the radiative transfer characteristics of the jet if the gamma and alpha crystalline structures have significantly distinct optical properties.



Fig. 7. Spatial map of default NARJ solution for the alpha phase fraction of the 1.5- $\mu m$  particle group.

The two larger particle groups experience greater drag force per particle, resulting in decreased cooling rates and velocities. Therefore, the particle phase change solidification process is pushed farther downstream beyond  $20 R_e$  axial distance.

The NARJ model was modified to replace the Russian-based chemical reaction rates with a common set of chemical equations and rates based on Baulch, et al.<sup>13</sup> The temperature-dependent rate equations and the associated rate coefficients are tabulated in Table 4.

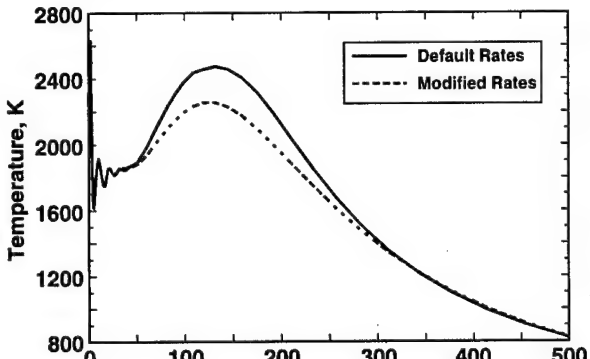
A comparison of the rate coefficients in Table 4 with those of Table 1 indicates that most rates are similar; however, some differences are noted. The most obvious is the exclusion of the nitrogen reaction set in the modified chemical equation set. Furthermore, the reactions leading to the exothermic formation of  $H_2O$  and  $CO_2$  are considerably faster in the default NARJ chemical rate system. The exception to this is the  $CO + O + M \rightarrow CO_2 + M$  reaction, in which the default NARJ rate is slower.

The global effect of the different kinetic reaction data is noted by contrasting NARJ solutions incorporating the default and modified rates.

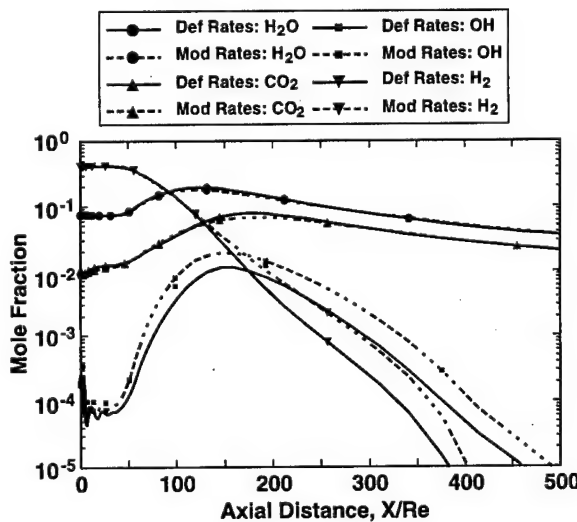
Table 4. Chemical Reaction Rate Coefficients used in the Modified NARJ Computations  $K^+ = AT^{-n} \exp(-E/RT)$

Reaction	$A, m^6/(kmol \cdot sec)^2$	$n$	$E, cal$
$H + H + M = H_2 + M$	1.09E+12	1	0
$H + O + M = OH + M$	3.63E+12	1	0
$O + O + M = O_2 + M$	1.09E+08	0	-1,800
$H + OH + M = H_2O + M$	1.09E+08	2	0
$CO + O + M = CO_2 + M$	1.09E+08	0	4,360
$Cl + Cl + M = Cl_2 + M$	2.36E+09	0	-1,800
$H + Cl + M = HCl + M$	3.63E+08	2	0
Reaction	$A, m^3/kmol \cdot sec$	$n$	$E, cal$
$OH + O = H + O_2$	1.81E+10	0	960
$OH + H = H_2 + O$	8.43E+06	-1	7,000
$OH + OH = H_2O + O$	6.02E+09	0	1,100
$H_2 + OH = H_2O + H$	2.11E+10	0	5,180
$OH + CO = CO_2 + H$	1.69E+04	-1.3	-660
$H_2O + Cl = HCl + OH$	8.43E+09	0	4,260
$HCl + O = OH + Cl$	3.01E+10	0	17,600
$H + Cl_2 = HCl + Cl$	3.61E+09	0	6,000
$H + Cl_2 = HCl + Cl$	9.03E+10	0	1,200

porating the default chemistry with the version of NARJ incorporating the modified rates. Figure 8a contrasts centerline axial profiles of the gas static temperature from NARJ solutions obtained with default and modified rates. The immediate near field results are identical, as the chemistry is essentially frozen until the mixing layer intersects the plume centerline at an axial distance of approximately  $50 R_e$ , denoting the beginning of the centerline afterburning region. The location where the mixing layer reaches the centerline is clearly evident in Fig. 8b, which compares the axial profiles of several chemically active species obtained from the default and the modified chemistry models. Based upon the depletion of  $H_2$  and the generation of  $H_2O$ , the afterburning region extends to approximately



a. Gas temperature



b. Gas composition

Fig. 8. Axial profiles on the jet centerline using the default NARJ rates and the modified rates.

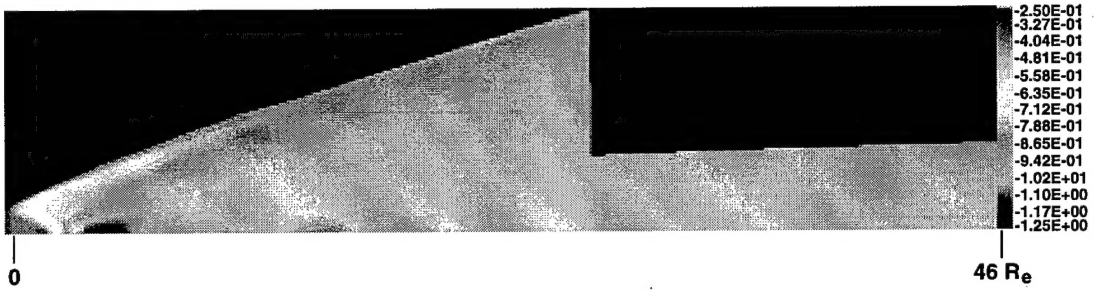


Fig. 9. Predicted NARJ pressure map. The values are the logarithm of the pressure in atm.

300  $R_e$  in both simulations. However, the NARJ default chemistry generates consistently higher gas temperatures. Downstream of the afterburning region, diffusive cooling dominates the flow, and the two solutions approach the same temperature values. Thus, while the modified rates do significantly alter the gas temperature in the afterburning region and slightly modify the species concentrations, the different chemical equations and rates do not significantly alter the spatial location of the temperature maximum, nor the global structure and composition of the non-afterburning jet regions. For the sake of this comparative analysis, all subsequent NARJ solutions were obtained incorporating the modified reactions and rate coefficients.

In order to further assess the NARJ model, a computed near-field pressure map is shown in Fig. 9. The axial extent of Fig. 9 is 46  $R_e$ . The nozzle exit radius is 1 foot. The intensity values are displayed as the logarithm of the pressure in atmospheres. The NARJ solution indicates a wave propagation structure in the near field. Following the initial expansion region, the pressure is nearly equal to the ambient pressure in the remaining computational regions. The pressure downstream of 5  $R_e$ , is

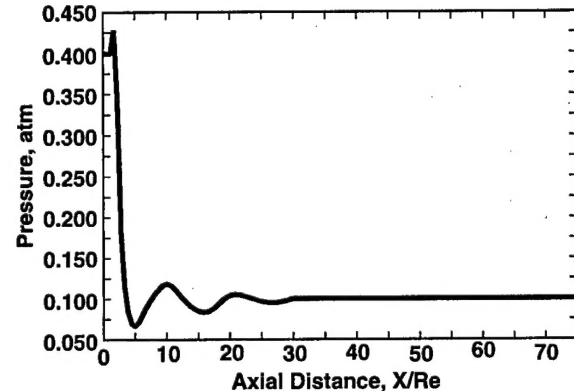


Fig. 10. NARJ axial profiles of the gas pressure on the jet centerline.

nearly equilibrated with the ambient pressure (Fig. 10) which displays the centerline axial gas static pressure profile. The small spike near 2  $R_e$  is evidence of a pressure wave caused by the initiation of burning in the shear layer immediately downstream of the nozzle exit. Following the precipitous pressure drop, the NARJ centerline result oscillates about the ambient pressure.

Figure 11 shows the NARJ gas temperature contour. The axial extent of the temperature contour map is 46  $R_e$ . Note that the NARJ radial temperature profiles have a local minimum on the cen-

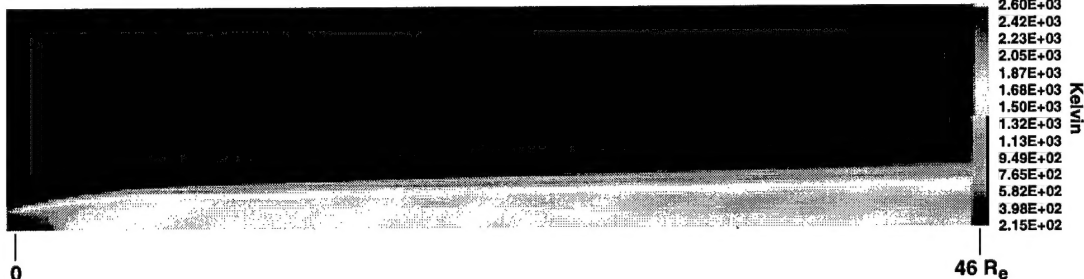


Fig. 11. Predicted NARJ temperature map.

terline with a local maximum at the shear layer for axial distances less than  $50 R_e$ .

The centerline temperature profiles of gas and particulates are shown in Fig. 12. The relatively low NARJ gas temperature allows the solid phase transition to occur in the smallest particle groups near the nozzle exit plane, as the temperature drops below 1,900 K in this region. Thus, in this simulation, both the 1.5- $\mu\text{m}$  radius and the 3.0- $\mu\text{m}$  radius particle groups undergo liquid to solid transitions prior to the occurrence of the afterburning region. The current NARJ model does not incorporate a mechanism allowing the solid particulates to remelt to the liquid phase, a phenomenon which could potentially occur in downstream combustion regions. The absence of the second phase change process could artificially enhance the proportion of the alpha solid phase in the downstream region.

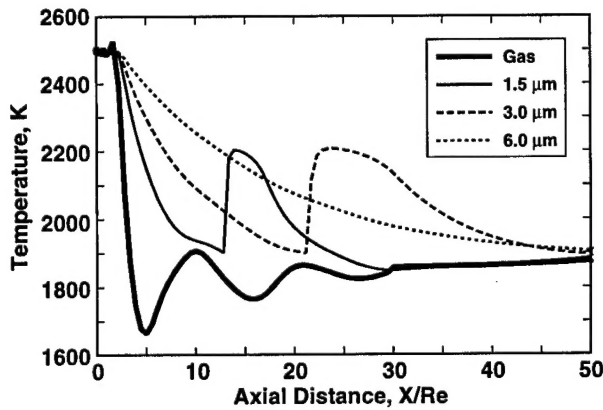


Fig. 12. NARJ axial profiles of the gas and particle temperatures on the jet centerline.

Figure 13 shows the centerline temperature profiles of the NARJ particles and gas for the complete solution extending to  $500 R_e$ , while Figure 14 is the centerline axial profiles of the mole fractions of  $\text{N}_2$  and  $\text{OH}$ . The axial location for the appearance of  $\text{N}_2$  is in keeping with the axial location of the centerline temperature rise, indicating the first occurrence of the shear layer mixing at the centerline. This temperature rise delays the phase transition of the largest particle group to downstream of the afterburning region.

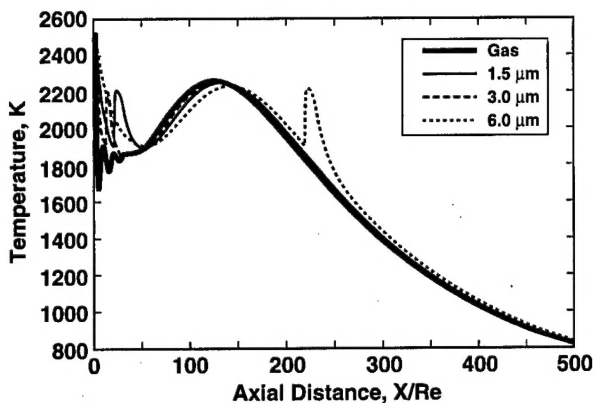


Fig. 13. The NARJ axial profiles of the gas and particle temperatures on the jet centerline, using the modified NARJ rates.

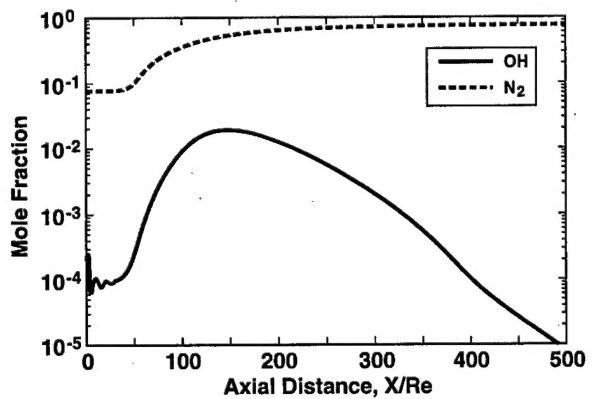


Fig. 14. NARJ axial profiles of the  $\text{OH}$  and  $\text{N}_2$  mole fractions on the jet centerline, using the modified NARJ rates.

## Conclusions

This work describes and demonstrates a comprehensive computational methodology for simulating the jet flow-field properties of multiphase, chemically reacting, aluminum-loaded propulsion-generated exhaust. The NARJ model incorporates a wide range of physical phenomena, including vibrational relaxation and vapor condensation, which were not explicitly discussed in this work. Physical approximations incorporated into the model include coupled temperature-dependent chemical kinetic rates, two-phase gas/particle drag, and turbulent mixing and particle phase change thermodynamics including supercooling phenomena. The NARJ methodology solves the inviscid and viscous flow regions using a unified approach. It also includes a

two-step kinetic  $\text{Al}_2\text{O}_3$  particle phase change model in which the phase change process includes an initial transition from liquid to solid metastable gamma crystalline structure immediately followed by a kinetic controlled rate transition to the stable alpha solid phase crystalline form. The transition from gamma to alpha is temperature dependent, occurs rapidly at elevated temperatures, and is extremely slow at moderate temperate ranges. Therefore, the majority of the solid  $\text{Al}_2\text{O}_3$  in jet flows is predicted by NARJ to be in the metastable gamma phase. These studies conclude that the crystalline structure formation does not significantly influence the gas dynamic properties; however, it could be an issue for radiative transfer simulations if the gamma and alpha phases have substantially different optical properties.

### Acknowledgements

The authors wish to acknowledge Dale Bradley for his assistance in the acquisition of the NARJ computer program at the Advanced Missile Signature Center. The technical assistance of Robert A. Reed concerning the radiative behavior of the alumina particles in the NARJ model and David W. Pruitt concerning the gasdynamics of the example problem is also acknowledged.

### References

1. *Thermodynamic and Thermophysical Properties of Combustion Products*. Handbook in 10 volumes, edited by Glushko, V. P., M., VINITI, Ac. of Science 1971, 1979 (translated in English from Russian, printed in Jerusalem by Kerer Press, 1974).
2. *Tactical Missile Aerodynamics*. Edited by Hemsch, M. J. and Nielsen, J. N., AIAA, New York, 1986.
3. *Thermodynamic Properties of Individual Materials*. Handbook in 4 volumes, edited by Glushko, V. P., M., Nauka, 1978-1982.
4. Molchanov, A. M., "Application of the Implicit McCormack Method to the Computation of Supersonic Turbulent Jets, Using an Algebraic Stress Model," Second Japan-Soviet Union Symposium on Computational Fluid Dynamics, August 27-31, 1990, pp. 231-238.
5. Henderson, C. B., "Drag Coefficient of Spheres in Continuum and Rarefied Flows," *AIAA Journal*, Vol. 14, No. 6, June 1976, pp. 707-708.
6. Hilling, W. B. and Turnbull, D., "Theory of Crystal Growth in Undercooled Pure Liquids," *J. Chem. Physics*, Vol. 24, 1956, p. 914.
7. Rosner, D. E. and Epstein, M., "Simultaneous Kinetic and Heat Transfer Limitations in the Crystallization of Highly Undercooled Melts," *Chemical Engineering Science*, Vol. 30, 1975, pp. 511-520.
8. Levi, C. G., Jayaram, V., Valencia, J. J., and Mehrabian, R., "Phase Selection in Electro-hydrodynamic Atomization of Alumina," *J. Mater. Res.*, Vol. 3, No. 5, 1988, pp. 969-983.
9. Steiner, C.J.-P., Hasselman, D.P.H., and Spriggs, R. M., Kinetics of Gamma-to-alpha alumina Phase Transformation," *Journal of the American Ceramic Society - Discussions and Notes*, 1971, Vol. 54, No. 8, pp. 412-413.
10. Plastinin, Yu. A., Anfimov, N. A., Baula, G. G., Karabadzhak, G. F., Khmelinin, B. A., and Rodionov, A. V., "Modeling of Aluminum Oxide Particle Radiation in a Solid Propellant Motor Exhaust," AIAA Paper No. 96-1879, 1996.
11. Rodionov, A. V., "A Godunov's Method Modification for Prediction of Supersonic Reacting Turbulent Jets," *La Recherche Aérospatiale*, No. 4, 1995, pp. 263-276.
12. Dash, S. M., Wolf, D. E., and Seiner, J. M., "Analysis of Turbulent Under-expanded Jets, Part

I, Parabolized Navier-Stokes Model, SCIPVIS,"  
*AIAA Journal*, Vol. 22, April 1995, pp. 505-514.

13. Baulch, D. L., Cox, R. A., Crutzen, P. J.,  
Hampson, R. F., Kerr, J. A., Troe, J., and Watson,  
R. T., *J. Phys. Chem. Ref. Data*, Vol. 11, 1982, p.  
327.